Extracting photoelectron spectra from the time-dependent wave function. II. Validation of two methods: Projection on plane waves and time-dependent surface flux

B. Fetić,[1,*] M. Tunja,[1] W. Becker,[2] and D. B. Milošević[1,3,2]

[1]*University of Sarajevo, Faculty of Science, Zmaja od Bosne 35, 71000 Sarajevo, Bosnia and Herzegovina*

[2]*Max-Born-Institut, Max-Born-Strasse 2a, 12489 Berlin, Germany*

[3]*Academy of Sciences and Arts of Bosnia and Herzegovina, Bistrik 7, 71000 Sarajevo, Bosnia and Herzegovina*

(Received 28 March 2022; accepted 10 May 2022; published 26 May 2022)

Extraction of the photoelectron spectrum (PES) from the time-dependent wave-packet calculations is a fundamental requirement for studying strong-field ionization. To analyze the PES, one needs to extract the physical observables from the time-dependent wave function at the end of the laser pulse. The exact PES can be obtained by projecting this wave function onto the continuum states of the same binding potential, which have to obey the incoming boundary condition. This means that the continuum states at large distances from the atomic or molecular targets have to be localized in momentum space so that asymptotically the continuum states can be approximated by plane waves. In this paper, we extend our previous analysis [B. Fetić, W. Becker, and D. B. Milošević, Extracting photoelectron spectra from the time-dependent wave function: Comparison of the projection onto continuum states and window-operator methods, Phys. Rev. A **102**, 023101 (2020)] and investigate two alternative methods of the PES extraction: projecting the time-dependent wave function onto plane waves as well as the so-called time-dependent surface flux (tSURFF) method. A thorough analysis is performed to check the reliability of these methods in comparison with the exact method. The time integral, which appears in the tSURFF ionization amplitude, is divided into smaller time intervals. Analyzing the corresponding partial amplitudes and their interference we relate these time intervals to particular parts of the PES. The method is applied to analyze the high-energy PES as well as the low-energy and very-low-energy structures in the PES.

DOI: 10.1103/PhysRevA.105.053121

I. INTRODUCTION

Studying the wave-packet dynamics of photoelectrons emitted from atomic or molecular targets irradiated by a strong laser field is essential for our understanding of the physical mechanisms of strong-field photoionization and related phenomena. The development of an accurate description of the wave-packet propagation by *ab initio* methods is a crucial element, but it is not the only one. Propagation of the initial bound-state wave function under the influence of a strong laser field is only the first challenge. In a photoionization experiment, the momentum and energy distributions of the photoelectrons are the experimental observables; thus the question arises how to obtain the energy-domain quantities from the time-dependent wave function represented on a spatial grid. Extraction of the photoelectron spectrum (PES) can be a challenging and computationally demanding task. The ever-increasing wavelengths and intensities of the lasers used in the strong-field ionization experiments and their simulations by *ab initio* methods have led to the development of numerous techniques for the PES calculation. Here we mention a few numerical methods which are different from those we are using, for example, the mask method [1–3], using the Kramers-Henneberger frame of reference for the evaluation of the electron spectra [4,5], and solving the time-dependent Schrödinger equation (TDSE) directly in the momentum space [6,7]. For a comprehensive review of the various numerical methods used in strong-field physics, see Ref. [8].

To accurately predict the PES from the wave-packet dynamics, the corresponding freely propagating photoelectron wave packet needs to be represented asymptotically by a superposition of plane waves with momenta close to the momentum measured at the detector, since plane waves are the eigenfunctions of the momentum operator. In our previous paper [9] we investigated the importance of using continuum states that satisfy the proper boundary condition to extract the PES from the time-dependent wave function obtained by numerical solution of the TDSE. The main conclusion of this paper was that the window-operator method, which has been used for three decades for obtaining the PES, may give artificial results for the photoelectron momentum distributions due to a wrong boundary condition imposed on the final photoelectron continuum wave function. Therefore, whenever an approximative method is used for calculating the PES, it has to be validated by direct comparison with the results obtained using the correct method: projecting the final time-dependent wave function onto continuum states obeying the correct, incoming-wave, boundary condition.

In this paper, we continue our analysis by investigating and validating two additional techniques for extracting the PES:

*benjamin.fetic@pmf.unsa.ba

the method of projecting the time-dependent wave function onto plane waves and the so-called time-dependent surface flux method (tSURFF). Comparisons with the exact results are presented and a detailed analysis for various targets and laser-field parameters is provided. In addition, the tSURFF method is used to investigate the buildup of interference structures in the time domain by analyzing the photoelectron flux through a spherical surface at a large distance from the atomic center. With this analysis, we are able to identify the wave packets that are responsible for some particular interference structures that show in the PES.

The paper is organized as follows. In Sec. II we give a brief introduction to the numerical methods that we use to propagate the wave function and to extract the corresponding physical quantities. In Sec. III we present our methods for extracting the photoelectron spectra. In Sec. IV we present and discuss our numerical results. In particular, in Secs. IV C and IV D we introduce a method for the time-energy-resolved analysis of the PES and apply it to investigate the corresponding high-energy and low-energy structures. Our conclusions are given in Sec. V. Atomic units ($\hbar = 1$, $4\pi\varepsilon_0 = 1$, $e = 1$, and $m_e = 1$) are used throughout the paper, unless otherwise stated.

II. PROPAGATION OF THE WAVE FUNCTION

The laser-atom interaction within the single-active-electron (SAE) approximation is described by the three-dimensional TDSE:

$$i\frac{\partial\Psi(\mathbf{r},t)}{\partial t} = [H_0 + V_I(t)]\Psi(\mathbf{r},t), \quad H_0 = -\frac{1}{2}\nabla^2 + V(r), \tag{1}$$

where H_0 is the field-free (atomic) Hamiltonian, $\boldsymbol{\nabla} \equiv \partial/\partial\mathbf{r}$, and $V(r)$ is the spherically symmetric binding potential

$$V(r) = -\frac{1}{r} + V_s(r), \tag{2}$$

which consists of the Coulomb potential and a short-range potential $V_s(r)$. For negative atomic ions, the Coulomb potential is absent so that $V(r) = V_s(r)$. The laser-atom interaction operator $V_I(t) = -iA(t)\partial_z$ is written in the dipole approximation and velocity gauge. Here we assume that the laser field is linearly polarized along the z axis, so that the vector potential is given by $A(t) = -\int^t E(t')dt'$, where $E(t)$ is the electric field:

$$E(t) = E_0 \sin^2\left(\frac{\omega t}{2N_c}\right)\cos(\omega t), \quad t \in [0, T_p], \tag{3}$$

with E_0 the electric-field amplitude, $\omega = 2\pi/T$ the laser-field frequency, and $T_p = N_c T$ the pulse duration (N_c is the number of optical cycles).

The TDSE is solved by expanding the time-dependent wave function in a basis of B-spline functions and spherical harmonics:

$$\Psi(r,\Omega,t) = \sum_{j=2}^{N-1}\sum_{\ell=0}^{L-1} c_{j\ell}(t)\frac{B_j(r)}{r}Y_\ell^{m_0}(\Omega), \tag{4}$$

where the expansion coefficients $c_{j\ell}(t)$ are time dependent, N is the number of B-spline functions in the domain $[0, r_{\max}]$, and $Y_\ell^m(\Omega)$ are the spherical harmonics, with $\Omega \equiv (\theta, \varphi)$ the solid angle. For a linearly polarized field, the magnetic quantum number is constant and we set it equal to $m_0 = 0$. Under the influence of the laser field, an electron, initially in a bound state, can be liberated from the atomic center and end up in the continuum. The continuum part of the wave packet is further accelerated by the electric force of the laser field. When the laser field is turned off, this part of the wave packet continues to propagate by moving away from the atomic (ionic) center as shown in Fig. 1. Outside the vicinity of the atom (called the reaction zone), the short-range potential falls off very quickly and beyond $r \geqslant R_c$ the wave packet propagates solely under the influence of the Coulomb potential. At some large distance from the atom, for $r \geqslant R$, the long-range Coulomb potential can be neglected and the wave packet can be considered as moving freely without any interaction with the atomic core. In a photoionization experiment, we measure the photoelectron momentum, so that the wave packet associated with the detected photoelectron must be localized in the momentum space. This implies that a freely propagating wave packet must (asymptotically) be represented by a superposition of plane waves with momenta close to that registered at the detector.

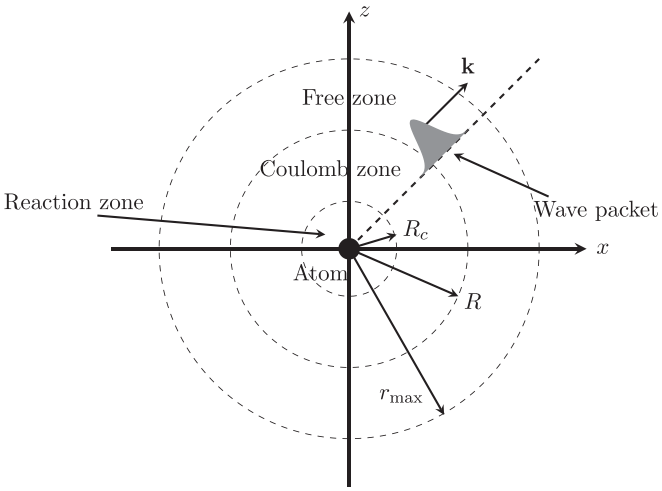

FIG. 1. At the end of the laser-atom interaction, the liberated part of the wave packet moves away from the vicinity of the atom (Reaction zone). As it further propagates, the short-range potential falls off very quickly and for $r > R_c$ the wave packet only feels the Coulomb potential (the Coulomb zone). At some large distance $r > R$ from the atom, the Coulomb potential can be neglected and the wave packet can be considered as a plane wave having linear momentum $\mathbf{k}$ (Free zone).

The TDSE (1), which describes the propagation of the wave packet, is numerically solved in a spherical box of the size $r = r_{\max}$ using the methods described in detail in Ref. [9]. Artificial reflections from the boundary at $r = r_{\max}$ are suppressed by the complex absorbing potential [10]:

$$V_{\mathrm{CAP}}(r) = \begin{cases} 0, & r < r_0 \\ -iV_0\left(\frac{r-r_0}{r_{\max}-r_0}\right)^2, & r_0 \leqslant r \leqslant r_{\max} \end{cases}, \tag{5}$$

with $V_0 = 0.1$ and $r_{\max} - r_0 = 100$.

III. CALCULATION OF THE PHOTOELECTRON SPECTRUM

A. Projection onto continuum states and plane waves

At the end of the laser field at the time $t = T_p$, using the propagation method described above, we obtain the time-dependent complex wave function $\Psi(\mathbf{r}, T_p)$. Then the exact photoelectron momentum distribution (PMD) can be calculated by projecting $|\Psi(T_p)\rangle$ onto the continuum states of the field-free Hamiltonian H_0 with linear momentum $\mathbf{k} = (k, \Omega_\mathbf{k})$, $\Omega_\mathbf{k} \equiv (\theta_\mathbf{k}, \varphi_\mathbf{k})$. These continuum states have to obey the so-called incoming boundary condition [11]. Therefore, the probability $P(E_\mathbf{k}, \theta_\mathbf{k})$ of detecting the electron with the kinetic energy $E_\mathbf{k} = \mathbf{k}^2/2$ emitted in the direction $\theta_\mathbf{k}$ is given by

$$P(E_\mathbf{k}, \theta_\mathbf{k}) = 2\pi k |\langle \psi_\mathbf{k}^{(-)} | \Psi(T_p)\rangle|^2, \tag{6}$$

where $k_x = k \sin\theta_\mathbf{k}$ and $k_z = k\cos\theta_\mathbf{k}$. The continuum states $\psi_\mathbf{k}^{(-)}(\mathbf{r})$ can be written as the partial wave expansion

$$\psi_\mathbf{k}^{(-)}(\mathbf{r}) = \sqrt{\frac{2}{\pi}} \frac{1}{k} \sum_{\ell,m} i^\ell e^{-i\Delta_\ell} \frac{u_\ell(k, r)}{r} Y_\ell^m(\Omega) Y_\ell^{m*}(\Omega_\mathbf{k}), \tag{7}$$

where $u_\ell(k, r)$ is the solution of the radial Schrödinger equation for fixed orbital quantum number ℓ and momentum k and Δ_ℓ is the scattering phase shift of the ℓth partial wave. The continuum states (7) are normalized on the momentum scale, i.e., $\langle \psi_{\mathbf{k}'}^{(\pm)} | \psi_\mathbf{k}^{(\pm)} \rangle = \delta(\mathbf{k}' - \mathbf{k})$. The wave packet formed by the continuum states (7) approaches a wave packet formed by the plane waves $\phi_\mathbf{k}(\mathbf{r}) = (2\pi)^{-3/2} e^{i\mathbf{k}\cdot\mathbf{r}}$ in the limit where $t \to +\infty$ [9,11,12]. The states $\psi_\mathbf{k}^{(+)}$ (see below) do not satisfy this requirement. We call this method the projection onto continuum states (PCS) method.

As explained in Ref. [9] and in Sec. 4 of Ref. [11], only the wave packet $\Psi_\mathbf{k}^{(-)}(\mathbf{r}, t) \equiv \int dk' C_k(k') e^{-iE_{\mathbf{k}'}t} \psi_{\mathbf{k}'}^{(-)}(\mathbf{r})$, with $C_k(k')$ an envelope function peaked at $k' = k$, is suitable for describing an ionization experiment. The reason is that in such an experiment the ionized electrons, having the linear momentum $\mathbf{k}$ and described by the wave packet $\Phi_\mathbf{k}(\mathbf{r}, t) \equiv \int dk' C_k(k') e^{-iE_{\mathbf{k}'}t} \phi_{\mathbf{k}'}(\mathbf{r})$, are registered at the detector after the ionization has occurred. Macroscopically, this electron is detected at the time $t \to +\infty$. After a lengthy calculation (see Sec. 4.2 in Ref. [12]) it can be shown that $\Psi_\mathbf{k}^{(-)}(\mathbf{r}, t) \xrightarrow{t\to\infty} \Phi_\mathbf{k}(\mathbf{r}, t = +\infty)$, which justifies our statements. On the other hand, forming the analogous wave packet with the so-called $\psi_\mathbf{k}^{(+)}$ states, which are also continuum eigenstates of the Hamiltonian H_0 but satisfy the outgoing boundary condition, one obtains $\Psi_\mathbf{k}^{(+)}(\mathbf{r}, t) \xrightarrow{t\to\infty} \Phi_\mathbf{k}(\mathbf{r}, t = +\infty)$ plus a scattering wave. Such states are suitable for the description of the final state in a scattering experiment but cannot be used in our case of ionization.

The advantage of the PCS method is that there is no need for additional postpulse propagation so that it poses lesser demands on the box size. On the other hand, an analytical solution for the continuum states is known only for the pure Coulomb potential. Continuum states for more complex atoms, modeled within the SAE approximation, have to be obtained numerically. This shortcoming of the PCS method can be overcome by further propagating the time-dependent wave function for some time τ after the laser field has been turned off. Mathematical details and an analysis of this method are discussed in Ref. [13]. The general idea is to postpulse propagate $\Psi(\mathbf{r}, T_p)$ under the influence of the field-free Hamiltonian H_0 for some time τ so that even the slowest part of the wave packet has reached the free zone. In that case, the PMD can be calculated by projecting out the bound part of the wave packet $\Psi(\mathbf{r}, T_p + \tau)$ and projecting only the continuum part onto the plane wave:

$$P(E_\mathbf{k}, \theta_\mathbf{k}) \approx P'(E_\mathbf{k}, \theta_\mathbf{k}) = 2\pi k |\langle \phi_\mathbf{k} | \Psi'(T_p + \tau)\rangle|^2. \tag{8}$$

We call this the projection onto plane waves (PPW) method. The prime on the time-dependent wave function in (8) indicates that we take only the part of the wave function $|\Psi(T_p + \tau)\rangle$ that has reached beyond the outer border of the Coulomb zone, i.e., beyond $r = R$. The plane waves can be written as the partial wave expansion

$$\phi_\mathbf{k}(\mathbf{r}) = \sqrt{\frac{2}{\pi}} \sum_{\ell,m} i^\ell j_l(kr) Y_\ell^m(\Omega) Y_\ell^{m*}(\Omega_\mathbf{k}), \tag{9}$$

where $j_\ell(kr)$ is the spherical Bessel function of the order ℓ. Inserting (4) and (9) into (8) we obtain the following expression for the PMD:

$$P'(E_\mathbf{k}, \theta_\mathbf{k}) = \frac{4}{k} \left| \sum_{j,\ell} (-i)^\ell c_{j\ell}(T_p + \tau) Y_\ell^{m_0}(\Omega_\mathbf{k}) \times \int_R^{r_{\max}} j_\ell(kr) B_j(r) r\, dr \right|^2. \tag{10}$$

B. Time-dependent surface flux method

A method frequently used for calculating the PES is the so-called tSURFF method, which was introduced by Tao and Scrinzi [14] and followed up in numerous papers by various authors (for details, see Refs. [15–20]). The basic idea behind the tSURFF method is to obtain the ionization probability by integrating the time-dependent outgoing electron flux through a surface at some distance from the atomic center. In practice, this means that we do not require the knowledge of the time-dependent wave function at every spatial point, but only the part of it enclosed in a sphere of radius R, thus reducing the computational effort for obtaining the PMD. In this section, we introduce an implementation of the tSURFF method in connection with the B splines.

The ionization probability amplitude within the approximation used in the tSURFF method is given by [14]

$$a_\mathbf{k} = i \int_0^{T_t} dt \langle \chi_\mathbf{k}(t) | [H_V, \Theta(r - R)] | \Psi(t)\rangle, \tag{11}$$

where $\Theta(r - R)$ is the Heaviside step function, $H_V = -\frac{1}{2}\nabla^2 - i\mathbf{A}(t)\cdot\nabla$ is the Hamiltonian describing the motion of the electron in the laser field, and $\chi_\mathbf{k}(\mathbf{r}, t)$ is the corresponding Volkov wave function [21]:

$$\chi_\mathbf{k}(\mathbf{r}, t) = (2\pi)^{-3/2} e^{-iE_\mathbf{k}t + i\mathbf{k}\cdot[\mathbf{r} - \boldsymbol{\alpha}(t)]}, \tag{12}$$

where $\boldsymbol{\alpha}(t) = \int^t dt' \mathbf{A}(t')$ is the classical excursion of an electron in the laser field alone. [In the velocity gauge, the $\mathbf{A}^2(t)$ term has been removed by a contact transformation.] The upper limit T_t in (11) must be chosen so that even the slowest

part of the wave packet reaches the surface boundary at $r = R$. Therefore, the tSURFF method requires that we postpulse propagate the time-dependent wave function for some additional time interval τ after the laser field has been turned off, i.e., $T_t = T_p + \tau$. The Volkov wave function becomes a plane wave when the laser field is turned off.

Inserting the time-dependent wave function (4) and the Volkov wave function (12) into (11) we obtain the following expression for the ionization amplitude [18]:

$$
\begin{aligned}
a_{\mathbf{k}} = \frac{R}{\sqrt{2\pi}} \int_0^{T_t} dt\, e^{iE_{\mathbf{k}}t + ik\alpha(t)\cos\theta_{\mathbf{k}}} \\
\times \sum_{j,\ell} \Big\{ (-i)^{\ell+1} Y_\ell^{m_0}(\Omega_{\mathbf{k}}) \Big[j_\ell(kr) c_{j\ell}(t) \\
\times \left(\frac{d}{dr} - \frac{\ell+1}{r} \right) B_j(r) + 2iA(t) j_\ell(kr) \\
\times \left[c_{\ell-1}^{m_0} c_{j\ell-1}(t) + c_\ell^{m_0} c_{j\ell+1}(t) \right] B_j(r) \\
+ k j_{\ell+1}(kr) c_{j\ell}(t) B_j(r) \Big] \Big\} \Big|_{r=R},
\end{aligned}
\tag{13}
$$

with

$$
c_\ell^{m_0} = \sqrt{\frac{(\ell+1)^2 - m_0^2}{(2\ell+1)(2\ell+3)}}. \tag{14}
$$

Now we can define the probability of detecting an electron with the energy $E_{\mathbf{k}}$ in the direction $\theta_{\mathbf{k}}$:

$$
P(E_{\mathbf{k}}, \theta_{\mathbf{k}}) \approx P_t(E_{\mathbf{k}}, \theta_{\mathbf{k}}) = 2\pi k |a_{\mathbf{k}}|^2. \tag{15}
$$

The tSURFF method properly produces the PES if the surface boundary is sufficiently far away from the atomic center so that the influence of the residual ion on the propagating wave packet can be neglected. In our calculations we set $R = 600$. The upper limit for the time integration can be estimated by using the classical picture of the electron motion in the laser pulse as

$$
T_t \geqslant T_p + \frac{R}{k_{\min}}, \tag{16}
$$

where $k_{\min}$ is the minimal momentum that we want to resolve in our PMD calculations. As a technical detail we mention that, in order to avoid an artificial contribution to the time integral, the integrand in Eq. (13) should be multiplied by a Hanning window [18]:

$$
h(t) = \begin{cases} 1, & t < T_t/2, \\ 1 - \cos(2\pi t/T_t), & t \geqslant T_t/2. \end{cases} \tag{17}
$$

IV. RESULTS

A. Projection onto plane waves

Let us first consider photoionization of the negative atomic ion H^-. Within the SAE approximation the corresponding binding potential can be modeled with the short-range potential [22]

$$
V_s(r) = -1.1 \frac{e^{-r}}{r}, \tag{18}
$$

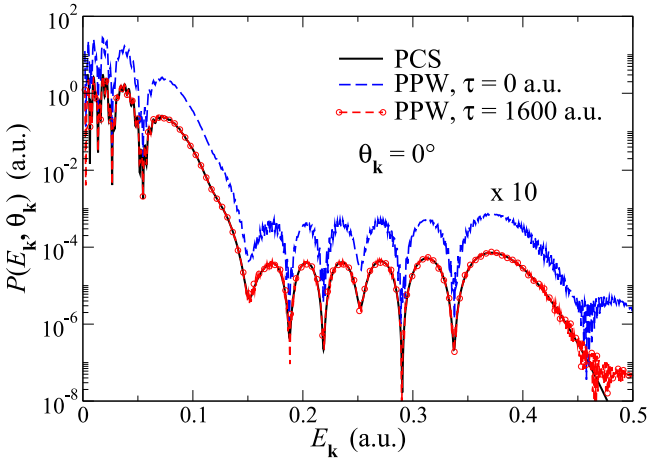

FIG. 2. Photoelectron spectra for the negative hydrogen ion H^- obtained by the PCS and PPW methods for $\theta_{\mathbf{k}} = 0°$. The exact PCS spectrum is represented by the solid black line, while the results obtained by the PPW method are given by the dashed blue line (for $\tau = 0$; the corresponding spectrum is shifted vertically for clarity) and by the dashed red line with circles (for $\tau = 1600$). The laser parameters are $I = 10^{11}$ W/cm^2, $\lambda = 10.8\,\mu$m, and $N_c = 4$. Note that the PCS and the PPW ($\tau = 1600$ a.u.) spectra are practically indistinguishable except at the highest energies.

which reproduces the ionization potential of the $1s$ ground state of H^-, which is equal to $I_p = 0.75$ eV. We use the following laser parameters: $I = E_0^2 = 10^{11}$ W/cm^2, $\lambda = 2\pi c/\omega = 10.8\,\mu$m, and $N_c = 4$. The ponderomotive energy for these field parameters is $U_p = E_0^2/(4\omega^2) = 0.038\,56$. In Fig. 2 we show the photoelectron spectrum in the direction $\theta_{\mathbf{k}} = 0°$, obtained by the PCS (solid black line) and PPW methods (dashed red line with circles and dashed blue line). Since there is no Coulomb potential, the Coulomb zone is absent and the free zone is very close to the atomic center. In the present calculations we set $R = 40$ and the radius of the spherical box is $r_{\max} = 4500$. The convergence of the numerical results was accomplished with $N = 12\,009$ B-spline functions and $L = 50$ spherical harmonics. From the results presented in Fig. 2, we see that the PPW spectrum obtained without postpulse propagation (dashed blue line) exhibits an artificial maximum in the high-energy region beyond the cutoff. This can be suppressed by using a longer postpulse propagation (dashed red line with circles), thus achieving better agreement with the PCS method in the high-energy region. The general rule for this kind of time-dependent calculations is that, with increasing postpulse propagation time τ, the agreement with the exact spectrum becomes better. This also implies that the radius of the spherical box $r_{\max}$ has to be large enough to enclose the entire wave function. Therefore, a compromise has to be made between the consumption of the computing resources and obtaining a photoelectron spectrum up to a desired kinetic energy. In Fig. 3, for another comparison, the PMDs obtained by these two methods are shown as color maps covering six orders of magnitude. Again, we see that these two methods produce identical PMDs. This conclusion also holds if we use another negative ion such as F^-. Details of this analysis can be found in Ref. [23].

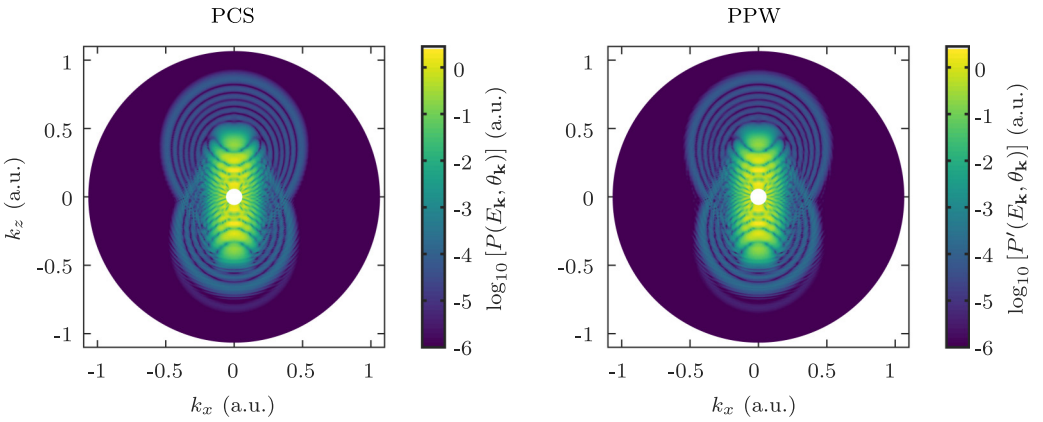

FIG. 3. The PMDs for the negative hydrogen ion H^- obtained by the PCS and PPW methods. The left panel shows the PMD obtained by the PCS method, while the right panel shows the PMD obtained by the PPW method with $\tau = 1600$. The laser parameters are the same as in Fig. 2.

As the second example, we use the Ar atom modeled by the one-electron potential [24]

$$V(r) = -\frac{1 + a_1 e^{-a_2 r} + a_3 r e^{-a_4 r} + a_5 e^{-a_6 r}}{r}, \qquad (19)$$

with $a_1 = 16.039$, $a_2 = 2.007$, $a_3 = -25.543$, $a_4 = 4.525$, $a_5 = 0.961$, and $a_6 = 0.443$. The ionization potential of the $3p$ ground state of Ar is $I_p = 15.774$ eV. In Fig. 4 we show the PMD obtained for the following laser parameters: $I = 7 \times 10^{13}$ W/cm^2, $\lambda = 800$ nm ($U_p = 0.15375$), and $N_c = 4$. Due to the long range of the Coulomb potential, the free zone boundary was set to $R = 60$ and, in order to achieve agreement with the exact spectrum, the postpulse time interval was increased to $\tau = 1800$. Again, we can see that the agreement of the results obtained using the PCS and PPW methods is more than satisfactory. The TDSE was solved using the numerical parameters $r_{\max} = 4000$, $N = 14\,009$, and $L = 40$.

In the case of atomic photoionization where the liberated electron moves in the modified Coulomb potential, a natural choice would be to use the Coulomb waves as an asymptotic approximation to the true continuum states. If we assume that the photoelectron moves in the long-range Coulomb field at the moment when it is detected, this will imply that the residual atomic (molecular) ion influences the detector and, in that case, the detected signal would be a consequence of the signal coming from the photoelectrons and the signal coming from the interaction with the ion. This is the main reason why the detectors are placed far away from the interaction region so that we can say with confidence that there are no additional signals recorded by the detectors except those coming from the photoelectrons. Hence, the Coulomb field cannot influence the photoelectrons in this region. We have explicitly shown that the results obtained by the PCS method at the instant when the laser field is turned off are the same as those obtained if we let the wave packet propagate freely to the detector and then use as the final wave function a plane wave with a well-defined momentum to obtain the differential ionization probability. However, the Coulomb waves behave asymptotically as plane waves only for very large distances, far beyond $R = 60$ as we used in our simulation. Therefore, projecting onto the Coulomb waves for R not large enough leads to incorrect results (in addition, the use of very large $r_{\max}$ to enclose the entire wave function is numerically too demanding). In this case, more satisfactory results are obtained by projecting

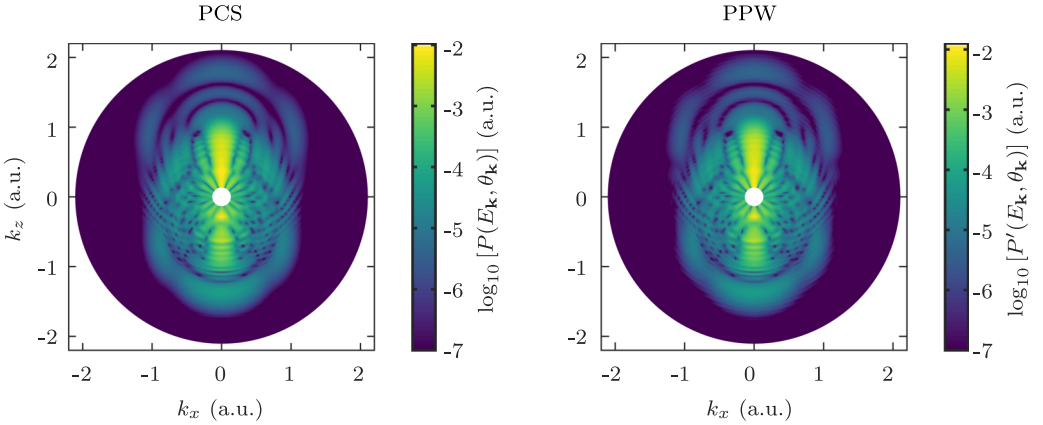

FIG. 4. The PMDs for the argon atom obtained by the PCS and PPW methods. The left panel shows the PMD obtained by the PCS method, while the right panel shows the PMD obtained by the PPW method with $\tau = 1800$. The laser parameters are $I = 7 \times 10^{13}$ W/cm^2, $\lambda = 800$ nm, and $N_c = 4$.

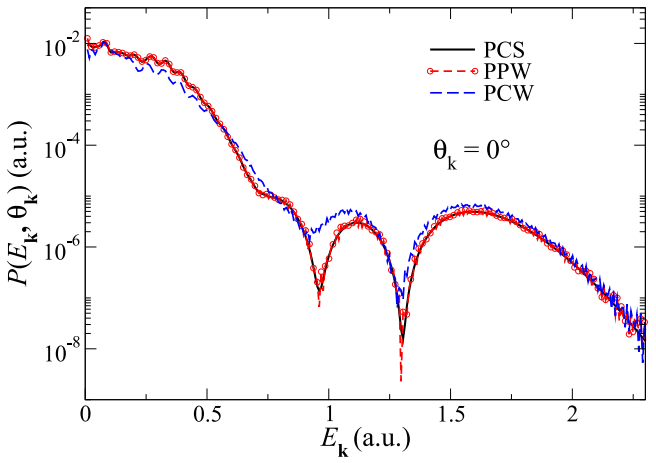

FIG. 5. Photoelectron spectra for the argon atom obtained by the PCS (solid black line), PPW (dashed red line with circles), and PCW (dashed blue line) methods for $\theta_k = 0°$. The PPW and PCW spectra are calculated for $R = 60$ and $\tau = 1800$. The laser parameters are the same as in Fig. 4. Note that throughout most of the plot the black line (PCS) is almost completely overlaid by the red line (PPW).

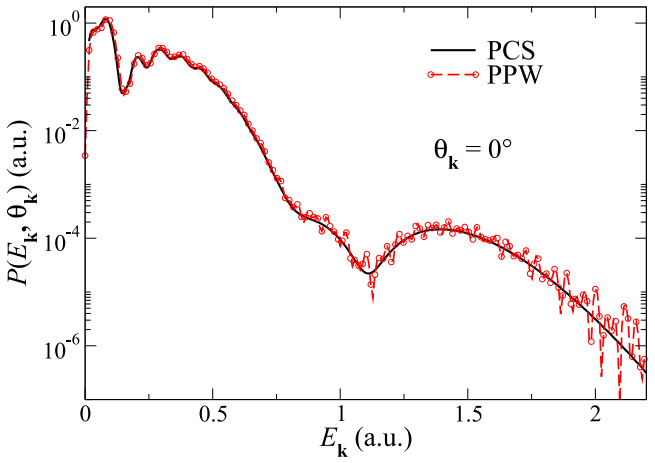

FIG. 6. Photoelectron spectra for the H_2^+ ion exposed to a laser pulse having the intensity $I = 10^{14}$ W/cm^2, wavelength $\lambda = 632$ nm, and total duration of $N_c = 4$ optical cycles. The solid black line depicts the exact spectrum, while the dashed red line with circles depicts the spectrum obtained by projecting the wave function onto plane waves, with the postpulse propagation time $\tau = 12T$.

onto plane waves, which are eigenstates of the momentum operator. This is illustrated in Fig. 5 where we show the photoelectron spectrum for the Ar atom in the direction of the laser-field polarization. The dashed blue line [projection onto Coulomb waves (PCW)] represents the spectrum calculated by projecting onto Coulomb waves within the free zone, while the dashed red line with circles (solid black line) specifies the spectrum obtained by the PPW (PCS) method. As can be seen from this plot, the PCW method gives the wrong spectrum, while the spectra obtained by the PCS method and the PPW method with $\tau = 1800$ agree quite well.

The PPW method, although computationally a very expensive method in terms of the box size, can be also applied for studying molecular systems. We applied this method to the molecular hydrogen cation H_2^+ exposed to a linearly polarized laser pulse having the intensity $I = 10^{14}$ W/cm^2, wavelength $\lambda = 632$ nm ($U_p = 0.1371$), and a total duration of $N_c = 4$ optical cycles. We assume that the laser-field polarization axis is parallel to the internuclear axis. The three-dimensional TDSE is numerically solved by expanding the time-dependent wave function in terms of the B-spline functions and expressing the spherical harmonics in prolate spheroidal coordinates within the fixed-nuclei approximation. The initial state is $1\sigma_u$ and the internuclear distance is 2 a.u. Details of the applied numerical method can be found in Refs. [25,26]. Calculated photoelectron spectra are shown in Fig. 6, where the solid black line represents the spectrum obtained by projecting the time-dependent wave function onto the two-center Coulomb wave function, whereas the dashed red line with circles depicts the spectrum obtained by projecting on plane waves, with the total postpulse propagation time $\tau = 12T$. Again, we see that the PPW and PCS methods give qualitatively the same photoelectron spectra. Therefore, regardless of the target, the PCS and PPW methods give the same results.

B. Photoelectron spectra with the tSURFF method

The postpulse propagation of the time-dependent wave function, used in the previous examples, leads to larger spatial grids in the numerical solution of the TDSE, effectively increasing the computational demands. This unfavorable feature of the PPW method can be overcome by using the tSURFF method, which is based on the calculation of the electron flux through a surface at a distance R from the atomic center. In this section, we show examples of PES and compare results obtained by the PCS and tSURFF methods. We use the argon atom as a benchmark case.

To test the reliability of the tSURFF method we increase the laser-pulse duration to $N_c = 12$ optical cycles while keeping the other laser parameters the same as in Fig. 4. In Fig. 7

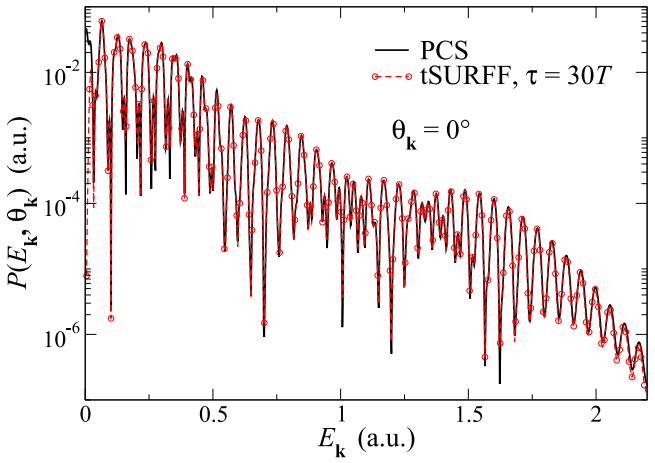

FIG. 7. Photoelectron spectra for the argon atom obtained by the PCS and tSURFF methods for $\theta_k = 0°$. The exact PCS spectrum is depicted by the solid black line, while the tSURFF spectrum is represented by the dashed red line with circles. The laser parameters are $I = 7 \times 10^{13}$ W/cm^2, $\lambda = 800$ nm, and $N_c = 12$.

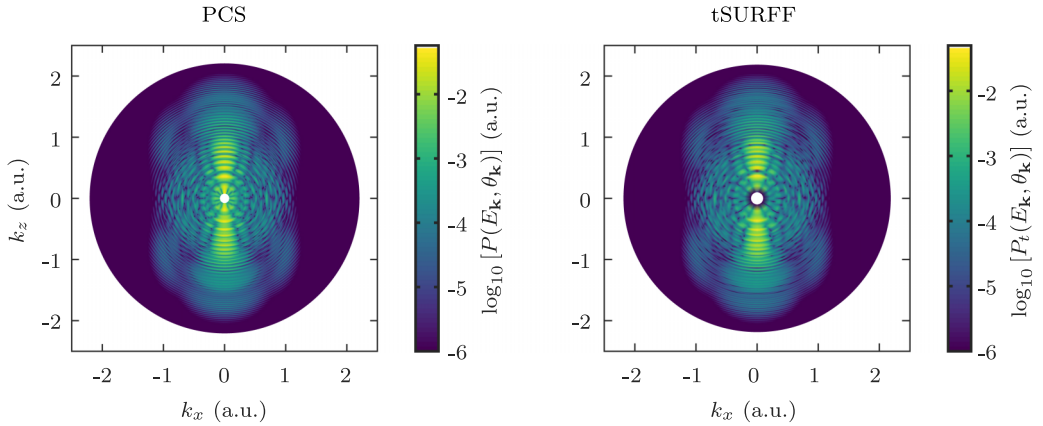

FIG. 8. The PMDs for the argon atom obtained by the PCS (left panel) and the tSURFF (right panel) methods. The laser parameters are the same as in Fig. 7.

we compare the PES obtained by the PCS method (black solid line) and the tSURFF method (dashed red line with circles) in the direction $\theta_\mathbf{k} = 0^\circ$. As we see, these two spectra completely overlap almost in the entire energy spectrum, except near the zero-energy region (this discrepancy can be corrected by further increasing the postpulse propagation time). The PCS spectrum is obtained by numerically solving the TDSE using up to $N = 10\,009$ B-spline functions, $L = 40$ spherical harmonics, and the spherical box of size $r_{\max} = 1800$. On the other hand, the tSURFF spectrum is obtained by solving the TDSE using $N = 4009$, $L = 40$, and $r_{\max} = 800$, with the postpulse propagation time $\tau = 30T$. Since the requirement for the spherical box size is reduced in the tSURFF calculations, the TDSE is numerically solved much faster if the PES is calculated with the tSURFF method (in comparison with the PCS method). This very useful feature of the tSURFF method becomes especially manifest for long and intense laser pulses in the near-infrared wavelength range where the liberated electron can travel a very large distance from the atomic core, thus requiring a very large spherical box to enclose the entire time-dependent wave function. In Fig. 8 we show the PMD velocity maps for the same parameters as in Fig. 7. They look the same, except again for very small momenta. Therefore, we conclude that the tSURFF method is a highly reliable and efficient method for calculating the PES if it is used properly.

C. Time-energy-resolved photoelectron spectrum

The interference of electron wave packets plays a crucial role in our understanding of the strong-field ionization process. Electron wave packets, liberated by the laser field at two different instants of time, follow different trajectories along which the electron wave packets accumulate different phases but can end up in a quantum state with the same final momentum. The wave packets are then coherently superimposed, leading to an interference pattern in the photoelectron momentum distribution. Examples of electron wave-packet interference patterns and the corresponding analysis can be found in Refs. [27–34].

A very intriguing feature of the tSURFF method is that it can be used to track the temporal interference of the electron wave packets as they pass through the surface at $r = R$. This surface can be viewed as a detector of the photoelectron wave packets. The temporal interference of the electron wave packets is incorporated in the time integral of the ionization amplitude (13). The time integration interval $[0, T_t]$ can be divided into N_t smaller intervals the contributions of which coherently add up:

$$a_\mathbf{k} = \sum_{i=1}^{N_t} a_{\mathbf{k}i} = \sum_{i=1}^{N_t} \int_{t_{i-1}}^{t_i} \tilde{a}_\mathbf{k}(t) dt, \tag{20}$$

where $\tilde{a}_\mathbf{k}(t)$ is the integrand in (13), $t_0 = 0$, and $t_{N_t} = T_t$. Each term in the sum substantially contributes to the ionization amplitude in a specific energy interval since it captures only those wave packets that pass through the surface during the time $t \in [t_{i-1}, t_i]$. This allows us to analyze the buildup of interference as it evolves in time. The ionization amplitude (13) can also be used to extract the time-energy resolved spectra with the help of the zero-frequency component of the Gabor transform, leading to a quasiprobability distribution in the energy-time domain [35].

In Fig. 9 we show the PES for the argon atom in the direction $\theta_\mathbf{k} = 0^\circ$ exposed to a laser pulse with the intensity $I = 1.5 \times 10^{14}$ W/cm^2, wavelength $\lambda = 800$ nm ($U_p = 0.32946$), and a total duration of $N_c = 4$ optical cycles. The solid black line represents the exact PES, while the dashed red line with circles represents the tSURFF spectrum obtained with the postpulse propagation time $\tau = 18T$. As we can see, these two curves completely overlap. Now, we closely examine the partial contributions to the PES using Eq. (20). We first divide the time integration interval $[0, T_t = 22T]$ into $N_t = 88$ subintervals, so that we can distinguish electron wave packets that pass through the surface during any one of the four quarters of the optical cycle. The solid blue line with squares $a_{\mathbf{k}17}$ shows the captured electron flux that passes through the surface in the time interval $t \in [4T, 4.25T]$. These are the fastest electrons, with energies beyond the classical cutoff, $E_\mathbf{k} > 10U_p$. On the other hand, the dashed blue line $a_{\mathbf{k}18}$ shows the contribution of the electron wave packets that pass through the surface in the interval $t \in [4.25T, 4.5T]$. The dash-dotted green line $a_{\mathbf{k}19}$ and solid purple line $a_{\mathbf{k}20}$ exhibit the contributions of the electrons passing through for $t \in [4.5T, 4.75T]$ and $[4.75T, 5T]$, respectively. The region

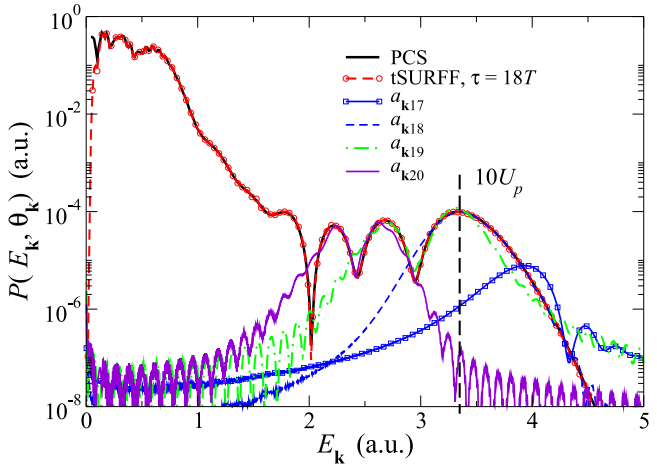

FIG. 9. Photoelectron spectra for the argon atom obtained by the PCS and tSURFF methods for $\theta_\mathbf{k} = 0°$. The exact spectrum and the spectrum obtained by the tSURFF method are depicted by the solid black line and the red line with circles, respectively. The solid blue line with squares and the dashed blue line show the contributions of the tSURFF spectrum for $t \in [4T, 4.25T]$ and $[4.25T, 4.5T]$, respectively. The dash-dotted green line and the solid purple line display the contributions of the electron wave packets registered in the time intervals $t \in [4.5T, 4.75T]$ and $[4.75T, 5T]$, respectively. The laser parameters are $I = 1.5 \times 10^{14}$ W/cm^2, $\lambda = 800$ nm, and $N_c = 4$.

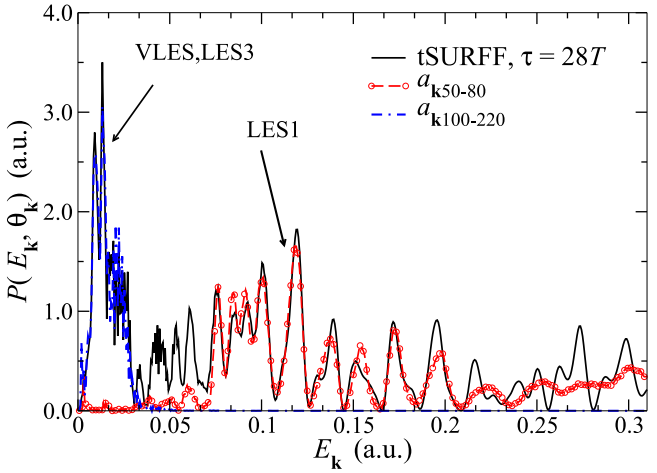

FIG. 10. Formation of the LES and VLES in the strong-field ionization spectrum of the argon atom exposed to a laser pulse with the intensity $I = 1.5 \times 10^{14}$ W/cm^2, wavelength $\lambda = 2000$ nm, and total duration of $N_c = 6$ optical cycles. The solid black line shows the full tSURFF spectrum in the direction $\theta_\mathbf{k} = 0°$. The red dashed line with the circles and the dashed blue line show the partial contributions to the spectrum from the electron wave packets passing the surface for times $t \in [49\frac{T}{8}, 80\frac{T}{8}]$ and $[99\frac{T}{8}, 220\frac{T}{8}]$, respectively.

near the classical cutoff at $10U_p$ can be explained by the interference of the wave packets corresponding to the partial contributions $a_{\mathbf{k}18}$ and $a_{\mathbf{k}19}$. The electron trajectories corresponding to these wave packets will have the same energy but will arrive at the detector at different times. The middle section of the plateau is produced mainly by the interference of the wave packets corresponding to the partial contributions $a_{\mathbf{k}19}$ and $a_{\mathbf{k}20}$ (solid purple line). The oscillatory character of the plateau that we observe can be explained by the beating of these partial contributions against each other. To conclude, the structure of the plateau can be reproduced almost completely by the interference of the electron wave packets that reach the surface in the time interval $t \in [4T, 5T]$. From the quantum-orbit analysis, we know that only two distinct orbits, the short and the long one, are responsible for the formation of the plateau and its structure in few-cycle laser pulses [29].

D. Low-energy structures

Finally, we investigate the so-called low-energy structure (LES) [36,37], called "ionization surprise" in Ref. [38], since it came as a surprise at a time when above-threshold ionization was believed to be completely understood. Moreover, the Keldysh-Faisal-Reiss theory [39–41], which had been expected to fully describe the low-energy (direct) part of the spectrum, failed to predict its existence. The LES manifests itself as a narrow enhancement in the photoelectron spectrum along the laser polarization axis direction at energies of a small fraction of the ponderomotive energy, about $0.1U_p$ and lower. Actually, there is a series of low-energy structures, called LES1, LES2, etc., at lower and lower energies. By now, there appears to be consensus that the LES is a rescattering phenomenon caused by forward-scattering trajectories the contributions of which are further enhanced by Coulomb focusing [42–44]. However, the LES is not a Coulomb effect *per se*. It is only strongly enhanced by the Coulomb field [45–47]. Another enhancement in the photoelectron spectrum at energies even lower than those of the LES, called the very-low-energy structure (VLES), was also observed [48,49]. While the LES can be traced to forward-scattered quantum orbits [46,47], the origin of the VLES is unclear. The cutoffs for the particular quantum orbits that generate the LES are at $0.094\,38U_p + 0.049\,53I_p$ for the LES highest in energy (the LES1) [at the intersection of the quantum orbits classified as $(\nu, \mu) = (\pm 1, 1)$] and at $0.032\,96U_p + 0.016\,76I_p$ for $(\nu, \mu) = (\pm 1, 2)$, $0.016\,68U_p + 0.008\,41I_p$ for $(\nu, \mu) = (\pm 1, 3)$, etc., for the LES2 and LES3 (see Table I in Ref. [50]); these values were obtained for an infinitely long (continuous wave) pulse and without taking into account Coulomb effects. Therefore, for the present paper, they can only serve as benchmark values.

Let us now investigate the buildup of the LES and VLES in time using the tSURFF method. In Fig. 10 we show the photoelectron spectra in the direction $\theta_\mathbf{k} = 0°$ for the laser parameters $I = 1.5 \times 10^{14}$ W/cm^2, $\lambda = 2000$ nm ($U_p = 2.0591$), and $N_c = 6$. The postpulse propagation time is $\tau = 28T$. As in the previous example, we divide the total time $T_t = 34T$ into $N_t = 272$ smaller time intervals so that we can distinguish electrons passing the surface down to one-eighth of an optical cycle. The TDSE is solved using $N = 4009$ B-spline functions and $L = 70$ spherical harmonics. The surface is set at $R = 600$ with the total spherical box extending up to $r_{\max} = 800$. The solid black line represents the spectrum obtained with the tSURFF method, while the dashed red line with circles represents the partial contribution to the spectrum from those wave packets that reach the surface in the time interval $t \in [49\frac{T}{8}, 80\frac{T}{8}]$. The electrons that form the LES1

pass the surface in this time interval. The dash-dotted blue line shows the partial contribution from the wave packets that reach the surface in the time interval $t \in [99\frac{T}{8}, 220\frac{T}{8}]$. These electrons contribute to the VLES, the LES3, and, possibly, the LES2. This analysis helps us to identify the times when the LES and the VLES are formed at the detector. We can now attribute other properties to the electron trajectories responsible for the LES and VLES since we know the time intervals when the various trajectories arrive at the detector.

V. CONCLUSIONS

We investigated and compared two different methods for the extraction of the photoelectron spectrum from the time-dependent wave packet calculated via numerical solution of the time-dependent Schrödinger equation. We showed that the photoelectron spectrum can, in principle, be obtained by approximating the exact continuum state of the field-free Hamiltonian obeying the incoming boundary condition with a plane wave having the linear momentum $\mathbf{k}$. Even though this approximation is appealing from the numerical point of view, it comes at an extra cost regarding the size of the spherical box. Namely, to obtain a converged photoelectron spectrum in the high-energy region, the wave function at the end of the laser-atom interaction has to be further propagated by the field-free Hamiltonian. This postpulse propagation requires that the spherical box be large enough to enclose the entire wave function.

Next, we used the tSURFF method to calculate the photoelectron spectrum. The results obtained were compared with the exact results. We showed that the time-dependent surface flux method is a reliable and very accurate method for calculating the photoelectron spectrum if it is used properly. Furthermore, we used the time-dependent surface flux method to track the buildup of the interference structure in the photoelectron spectrum as it evolves in time. We applied this method to investigate the buildup in time of the high-energy plateau and the cutoff PES as well as of the low-energy and very-low-energy structures in the photoelectron spectrum.

ACKNOWLEDGMENT

We acknowledge support by the Ministry for Science, Higher Education, and Youth of Canton Sarajevo, Bosnia and Herzegovina.

[1] S. Chelkowski, C. Foisy, and A. D. Bandrauk, Electron-nuclear dynamics of multiphoton H_2^+ dissociative ionization in intense laser fields, Phys. Rev. A **57**, 1176 (1998).

[2] X. M. Tong, K. Hino, and N. Toshima, Phase-dependent atomic ionization in few-cycle intense laser fields, Phys. Rev. A **74**, 031405(R) (2006).

[3] U. De Giovannini, D. Varsano, M. A. L. Marques, H. Appel, E. K. U. Gross, and A. Rubio, *Ab initio* angle- and energy-resolved photoelectron spectroscopy with time-dependent density-functional theory, Phys. Rev. A **85**, 062515 (2012).

[4] D. A. Telnov and S.-I Chu, Above-threshold-ionization spectra from the core region of a time-dependent wave packet: An ab initio time-dependent approach, Phys. Rev. A **79**, 043421 (2009).

[5] D. A. Telnov and S.-I Chu, Low-energy structure of above-threshold-ionization electron spectra: Role of the coulomb threshold effect, Phys. Rev. A **83**, 063406 (2011).

[6] Z. Zhou and S.-I Chu, Precision calculation of above-threshold multiphoton ionization in intense short-wavelength laser fields: The momentum-space approach and time-dependent generalized pseudospectral method, Phys. Rev. A **83**, 013405 (2011).

[7] Z. Zhou and S.-I Chu, Multiphoton above-threshold ionization in superintense free-electron x-ray laser fields: Beyond the dipole approximation, Phys. Rev. A **87**, 023407 (2013).

[8] *Computational Strong-Field Quantum Dynamics: Intense Light-Matter Interactions*, edited by D. Bauer (De Gruyter, Berlin, 2016)

[9] B. Fetić, W. Becker, and D. B. Milošević, Extracting photoelectron spectra from the time-dependent wave function: Comparison of the projection onto continuum states and window-operator methods, Phys. Rev. A **102**, 023101 (2020).

[10] D. Neuhasuer and M. Baer, The time-dependent Schrödinger equation: Application of absorbing boundary conditions, J. Chem. Phys. **90**, 4351 (1989).

[11] A. F. Starace, in *Handbuch der Physik*, Vol. 31, edited by W. Mehlhorn (Springer-Verlag, Berlin, 1982), pp. 1–121.

[12] P. Roman, *Advanced Quantum Theory: An Outline of the Fundamental Ideas* (Addison-Wesley, Reading, MA, 1965).

[13] L. B. Madsen, L. A. A. Nikolopoulos, T. K. Kjeldsen, and J. Fernández, Extracting continuum information from $\Psi(t)$ in time-dependent wave-packet calculations, Phys. Rev. A **76**, 063407 (2007).

[14] L. Tao and A. Scrinzi, Photo-electron momentum spectra from minimal volumes: the time-dependent surface flux method, New J. Phys. **14**, 013021 (2012).

[15] A. Scrinzi, t-SURFF: Fully differential two-electron photo-emission spectra, New J. Phys. **14**, 085008 (2012).

[16] V. V. Serov, V. L. Derbov, T. A. Sergeeva, and S. I. Vinitsky, Hybrid surface-flux method for extraction of the ionization amplitude from the calculated wave function, Phys. Rev. A **88**, 043403 (2013).

[17] F. Morales, T. Bredtmann, and S. Patchkovskii, iSURF: a family of infinite-time surface flux methods, J. Phys. B **49**, 245001 (2016).

[18] V. Mosert and D. Bauer, Photoelectron spectra with Qprop and t-SURFF, Comput. Phys. Commun. **207**, 452 (2016).

[19] Y. Orimo, T. Sato, and K. L. Ishikawa, Application of the time-dependent surface flux method to the time-dependent multiconfiguration self-consistent-field method, Phys. Rev. A **100**, 013419 (2019).

[20] V. Tulsky and D. Bauer, Qprop with faster calculation of photoelectron spectra, Comput. Phys. Commun. **251**, 107098 (2020).

[21] C. J. Joachain, N. J. Kylstra, and R. M. Potvliege, *Atoms in Intense Laser Fields* (Cambridge University, New York, 2011).

[22] N. B. Delone and V. P. Krainov, *Multiphoton Processes in Atoms*, 2nd ed. (Springer-Verlag, Berlin, 2000).

[23] K. Amini, A. Chacón, S. Eckart, B. Fetić, and M. Kübel, Quantum interference and imaging using intense laser fields, Eur. Phys. J. D **75**, 275 (2021).

[24] X. M. Tong and C. D. Lin, Empirical formula for static field ionization rates of atoms and molecules by lasers in the barrier-suppression regime, J. Phys. B **38**, 2593 (2005).

[25] B. Fetić and D. B. Milošević, Numerical solution of the time-dependent Schrödinger equation for H_2^+ ion with application to high-harmonic generation and above-threshold ionization, Phys. Rev. E **95**, 053309 (2017).

[26] B. Fetić and D. B. Milošević, High-order above-threshold ionization of the H_2^+ ion: The role of internuclear distance, Phys. Rev. A **99**, 043426 (2019).

[27] F. Lindner, M. G. Schätzel, H. Walther, A. Baltuška, E. Goulielmakis, F. Krausz, D. B. Milošević, D. Bauer, W. Becker, and G. G. Paulus, Attosecond Double-Slit Experiment, Phys. Rev. Lett. **95**, 040401 (2005).

[28] D. B. Milošević, G. G. Paulus, and W. Becker, Ionization by few-cycle pulses: Tracing the electron orbits, Phys. Rev. A **71**, 061404(R) (2005).

[29] D. B. Milošević, D. Bauer, and W. Becker, Quantum-orbit theory of high-order atomic processes in intense laser fields, J. Mod. Opt. **53**, 125 (2006).

[30] D. B. Milošević, G. G. Paulus, D. Bauer, and W. Becker, Above-threshold ionization by few-cycle pulses, J. Phys. B **39**, R203 (2006).

[31] D. G. Arbó, K. L. Ishikawa, K. Schiessl, E. Persson, and J. Burgdörfer, Diffraction at a time grating in above-threshold ionization: The influence of the Coulomb potential, Phys. Rev. A **82**, 043426 (2010).

[32] X.-B. Bian, Y. Huismans, O. Smirnova, K.-J. Yuan, M. J. J. Vrakking, and A. D. Bandrauk, Subcycle interference dynamics of time-resolved photoelectron holography with midinfrared laser pulses, Phys. Rev. A **84**, 043420 (2011).

[33] P. A. Korneev, S. V. Popruzhenko, S. P. Goreslavski, W. Becker, G. G. Paulus, B. Fetić, and D. B. Milošević, Interference structure of above-threshold ionization versus above-threshold detachment, New J. Phys. **14**, 055019 (2012).

[34] S. Borbély, A. Tóth, D. G. Arbó, K. Tőkési, and L. Nagy, Photoelectron holography of atomic targets, Phys. Rev. A **99**, 013413 (2019).

[35] V. A. Tulsky and D. Bauer, Numerical time-of-flight analysis of the strong-field photoeffect, Phys. Rev. Research **2**, 043083 (2020).

[36] C. I. Blaga, F. Catoire, P. Colosimo, G. G. Paulus, H. G. Muller, P. Agostini, and L. F. DiMauro, Strong-field photoionization revisited, Nat. Phys. **5**, 335 (2009).

[37] W. Quan, Z. Lin, M. Wu, H. Kang, H. Liu, X. Liu, J. Chen, J. Liu, X. T. He, S. G. Chen, H. Xiong, L. Guo, H. Xu, Y. Fu, Y. Cheng, and Z. Z. Xu, Classical Aspects in Above-Threshold Ionization with a Midinfrared Strong Laser Field, Phys. Rev. Lett. **103**, 093001 (2009).

[38] F. H. M. Faisal, Strong-field physics: Ionization surprise, Nat. Phys. **5**, 319 (2009).

[39] L. V. Keldysh, JETP **20**, 1307 (1965).

[40] F. H. M. Faisal, Multiple absorption of laser photons by atoms, J. Phys. B **6**, L89 (1973).

[41] H. R. Reiss, Effect of an intense electromagnetic field on a weakly bound system, Phys. Rev. A **22**, 1786 (1980).

[42] C. Liu and K. Z. Hatsagortsyan, Origin of Unexpected Low Energy Structure in Photoelectron Spectra Induced by Midinfrared Strong Laser Fields, Phys. Rev. Lett. **105**, 113003 (2010).

[43] T.-M. Yan, S. V. Popruzhenko, M. J. J. Vrakking, and D. Bauer, Low-Energy Structures in Strong Field Ionization Revealed by Quantum Orbits, Phys. Rev. Lett. **105**, 253002 (2010).

[44] A. Kästner, U. Saalmann, and J. M. Rost, Electron-Energy Bunching in Laser-Driven Soft Recollisions, Phys. Rev. Lett. **108**, 033201 (2012).

[45] L. Guo, S. S. Han, X. Liu, Y. Cheng, Z. Z. Xu, J. Fan, J. Chen, S. G. Chen, W. Becker, C. I. Blaga, A. D. DiChiara, E. Sistrunk, P. Agostini, and L. F. DiMauro, Scaling of the Low-Energy Structure in Above-Threshold Ionization in the Tunneling Regime: Theory and Experiment, Phys. Rev. Lett. **110**, 013001 (2013).

[46] W. Becker, S. P. Goreslavski, D. B. Milošević, and G. G. Paulus, Low-energy electron rescattering in laser-induced ionization, J. Phys. B **47**, 204022 (2014).

[47] W. Becker and D. B. Milošević, Above-threshold ionization for very low electron energy, J. Phys. B **48**, 151001 (2015).

[48] C. Y. Wu, Y. D. Yang, Y. Q. Liu, Q. H. Gong, M. Wu, X. Liu, X. L. Hao, W. D. Li, X. T. He, and J. Chen, Characteristic Spectrum of Very Low-Energy Photoelectron from Above-Threshold Ionization in the Tunneling Regime, Phys. Rev. Lett. **109**, 043001 (2012).

[49] B. Wolter, C. Lemell, M. Baudisch, M. G. Pullen, X.-M. Tong, M. Hemmer, A. Senftleben, C. D. Schröter, J. Ullrich, R. Moshammer, J. Biegert, and J. Burgdörfer, Formation of very-low-energy states crossing the ionization threshold of argon atoms in strong mid-infrared fields, Phys. Rev. A **90**, 063424 (2014).

[50] D. B. Milošević, Low-energy backscattering quantum orbits in above-threshold ionization, J. Phys. B **49**, 175601 (2016).